



Mixed mode transition in boundary layers: Helical instabilityRikhi Bose ^{1,2,*} and Paul A. Durbin ³¹*Max Planck Institute for Solar System Research, Göttingen 37077, Germany*²*Engineering Laboratory, National Institute of Standards & Technology, Gaithersburg, Maryland 20899, USA*³*Aerospace Engineering, Iowa State University, Ames, Iowa 50011, USA*

(Received 28 January 2024; accepted 22 May 2024; published 12 June 2024)

Recent [Bose and Durbin, *Phys. Rev. Fluids* **1**, 073602 (2016)] direct numerical simulations (DNS) of adverse- and zero-pressure-gradient boundary layers beneath moderate levels of free stream turbulence ($Tu \leq 2\%$) revealed a mixed mode transition regime, intermediate between orderly and bypass routes. In this regime, the amplitudes of the Klebanoff streaks and instability waves are similar, and both can contribute significantly as these interact. Three-dimensional visualizations of transitional eddies revealed a helical pattern, quite distinct from the sinuous and varicose forms seen in pure bypass transition. This raises the fundamental question of whether the helical pattern could be attributed to a previously unknown instability mode. In the present work, based on stability analyses, we show that it is indeed the case. Two-dimensional stability analyses are performed herein for base flows extracted from DNS flow fields. The three-dimensional structure of the eigenfunction of the most unstable mode indeed reveals a helical pattern. The instability arises well upstream of the appearance of helical structures in flow visualizations. In DNS, fluctuations at wavelengths corresponding to the instability modes have negligible energy in the upstream region. Due to their high growth rates, these instability modes develop into helical patterns in the transition region, which quickly break down. The streak configuration leading to the formation of the helical mode instability is different from those leading to sinuous and varicose modes, analyzed in previous studies of pure bypass transition. Thus, the mixed mode precursor is the distinctive cause of helical mode transition.

DOI: [10.1103/PhysRevFluids.9.063905](https://doi.org/10.1103/PhysRevFluids.9.063905)**I. INTRODUCTION**

Direct numerical simulations (DNS) have provided a detailed description of the laminar to turbulent transition process in attached subsonic boundary layers. Both orderly and bypass transition have been investigated in detail. The theory of orderly transition is well established. It starts with exponential growth of instability waves, followed by a much faster secondary instability process forming Λ vortices. Finally, lifted Λ vortices break down into patches of turbulence—that final stage is impervious to theory. When transition does not emerge from growing instability waves it is classified as bypass transition. In most of the literature, bypass transition is synonymous with transition due to incident free-stream turbulence (FST). Over time various theoretical concepts have emerged [1]. They explain the occurrence of streamwise elongated perturbations, called Klebanoff

*Contact author: rikhi.bose@gmail.com

streaks, as precursors to transition. These disturbances amplify via the lift up mechanism, or algebraic growth, until their amplitudes saturate. Klebanoff streaks undergo secondary instability. The nature of that secondary instability is less clear cut than the Λ vortices of orderly transition. Analysis have characterized it in terms of sinuous and varicose modes, and outer and inner instabilities [2,3].

Experimental evidence suggests the existence of flow regimes in which both instability waves and streaks are involved in the transition process [4,5]. Especially, this can occur in adverse pressure gradient (APG) under low to moderate levels of free-stream turbulence.

A recent DNS study [6–8] revealed an intriguing transition process: beneath moderate levels of FST (intensity $Tu \leq 2\%$), and in the presence of instability waves at super-critical Reynolds numbers, a truly mixed mode transition process was reported. Three-dimensional visualizations of the perturbation fields revealed features quite distinct from the sinuous and varicose modes of pure bypass transition. The flow structures resembled a helical pattern. A deep lying critical layer was reported for these helical eddies, and therefore, these were classified as inner instabilities—in the terminology of Vaughan and Zaki [9]—but, again, distinct from what had been seen previously.

Those empirical observations pose the fundamental questions, does a helical, secondary streak instability exist? and, is it the cause of the patterns seen in flow visualization? Those questions prompted the present study. We analyze the secondary stability of boundary layers in the mixed mode transition regime. Both zero and APG boundary layers are considered. The approach parallels that of Hack and Zaki [3]: observed helical patterns are tracked back in time to identify their precursors. These provide base flow fields to which stability analysis is applied. An iterative technique is used to extract those eigenmodes having the highest growth rates.

As will be shown, the eigenfunction solution that is obtained is indeed of helical form. These eigenmodes are obtained even for apparently innocuous base streaks, significantly earlier than the helical instability is seen in DNS. This substantiates the hypothesis that the helices that were seen in computer simulations can be attributed to a new type of instability.

In previous studies, outer sinuous and inner varicose streak instabilities have been attributed to the inflection points in the spanwise and wall-normal profiles of the streamwise velocity, respectively [2,3]. The inner helical mode appears at the intersection of low- and high-speed streaks, where spanwise and wall-normal shear are both important. Such unique orientation of the streaks is due to the high growth rate of the mixed mode precursors, formed as a consequence of the instability waves interacting with the Klebanoff streaks. As is inevitable, the new instability is a consequence of the precursor differing from previous studies.

II. NUMERICAL TECHNIQUES

A. Direct numerical simulations

Direct simulations of previous studies were repeated to create the precursor fields required for the present study. These are of mixed mode transition, for both ZPG and APG boundary layers. A detailed description of the numerical methods, boundary conditions, and the method for the generation of inlet turbulence can be found in [8,10] and are not repeated here. For all simulations, inlet FST with a prescribed intensity ($Tu \equiv \sqrt{\frac{1}{3}u_i' u_i'}/U_\infty = 1\%$ and 2% , where, u_i' is the perturbation velocity along the i th axis) is superimposed on a Blasius boundary layer [11,12] at a super-critical Reynolds number, $Re_b = \sqrt{U_\infty x_0}/\nu \approx 398$. Here, U_∞ is the free-stream flow speed, x_0 is the distance of the inflow plane from the leading edge of the plate, and ν is the kinematic viscosity. In ZPG simulations, the inlet additionally includes a Tollmien-Schlichting (TS) wave with amplitude $A = 0.5\%U_\infty$. The domain is rectangular for the ZPG simulations with size $320\delta_0 \times 24\delta_0 \times 24\delta_0$ (δ_0 is the boundary-layer thickness at inlet) in the streamwise, wallnormal, and spanwise directions. The grid has $1537 \times 161 \times 241$ points. The computational domain and grid specifications for the APG simulations are the same as the ZPG simulations except that the APG is induced by a curved upper boundary characterized by the Hartree parameter, $\beta_H = -0.14$ [8]. The largest grid spacings in viscous units are reported in Table I. Despite the use of different grids, the mean skin-friction curves

TABLE I. DNS: Largest grid spacings in viscous units.

PG	Tu	Δx_{\max}^+	$\Delta y_{1,\max}^+$	Δz_{\max}^+
APG	$1\%U_\infty$	18.73	0.994	8.99
APG	$2\%U_\infty$	18.83	0.987	9.04
ZPG	$1\%U_\infty$	20.71	0.97	9.94
ZPG	$2\%U_\infty$	20.4	0.95	9.79

from the present simulations are in good agreement with those from previous studies [7,8,10]. Once a statistically stationary state was reached in the simulations, instantaneous snapshots were stored at constant time intervals of $1.8\delta_0/U_\infty$, over a period spanning at least three flow-through times, for stability analysis.

B. Stability analysis

Base flow profiles are extracted in planes normal to the streamwise direction from instantaneous DNS fields. Only the streamwise component of the velocity field is included, $[\mathbf{U}_b, p_b] = [U_b(y, z; x, t), 0, 0]$. The x, t dependence is treated as parametric for the stability analysis. Perturbations are periodic in the streamwise direction, of the form

$$[\mathbf{u}'_2, p'_2](x, y, z, t) = [\hat{u}_2, \hat{v}_2, \hat{w}_2, \hat{p}_2](y, z, t)e^{ik_x x},$$

where k_x is the streamwise wave number, also extracted from the DNS. These idealizations can be formally justified, as the streaky base flow is predominantly in the streamwise direction, and changes far more slowly than the growth rate of the perturbations in x and t [2,3]. Consequently, the following set of coupled linear equations is obtained for the perturbations

$$(ik_x)\hat{u}_2 + \frac{\partial \hat{v}_2}{\partial y} + \frac{\partial \hat{w}_2}{\partial z} = 0, \quad (1)$$

$$\frac{\partial \hat{u}_2}{\partial t} = [-ik_x U_b + \Delta]\hat{u}_2 + \left[-\frac{\partial U_b}{\partial y}\right]\hat{v}_2 + \left[-\frac{\partial U_b}{\partial z}\right]\hat{w}_2 + [-ik]\hat{p}_2,$$

$$\frac{\partial \hat{v}_2}{\partial t} = [0]\hat{u}_2 + [-ik_x U_b + \Delta]\hat{v}_2 + [0]\hat{w}_2 + \left[-\frac{\partial}{\partial y}\right]\hat{p}_2, \quad (2)$$

$$\frac{\partial \hat{w}_2}{\partial t} = [0]\hat{u}_2 + [0]\hat{v}_2 + [-ik_x U_b + \Delta]\hat{w}_2 + \left[-\frac{\partial}{\partial z}\right]\hat{p}_2.$$

The Laplacian is $\Delta = \frac{1}{\text{Re}}(-k_x^2 + \frac{\partial^2}{\partial y^2} + \frac{\partial^2}{\partial z^2})$. $[0]$ indicates a zero in a matrix element of the discretized equations.

The perturbations satisfy the following boundary conditions:

$$\hat{u}_2, \hat{v}_2, \hat{w}_2 = 0 \quad \text{at } y = 0, \quad (3)$$

$$\frac{\partial \hat{u}_2}{\partial y}, \hat{v}_2, \frac{\partial \hat{w}_2}{\partial y} = 0 \quad \text{as } y \rightarrow \infty. \quad (4)$$

As in the DNS, a periodic boundary condition is applied in the spanwise direction.

It was checked whether the wall normal and spanwise velocity components of the streaks have any effect on the emergence of the helical instability. All three components for the base flow $[\mathbf{U}_b, p_b] = [U_b(y, z; x, t), V_b(y, z; x, t), W_b(y, z; x, t), 0]$ were added to the perturbation equations (1) and (2) for this check. The structure of the obtained eigenfunctions was essentially the same as the one-component base flow considered in the presented results. The highest deviation of

the frequency of the most unstable waves was $\sim 5\%$ from the one-component solution. The growth rate is more delicate, and growth rates were of similar magnitude, but higher. For our purpose, the mode shape and frequency—and hence, phase speed—are of greatest importance.

Following Barkley and Henderson [13], the set of autonomous equations may be written as

$$\frac{\partial \hat{\mathbf{u}}_2}{\partial t} = \mathbf{C} \hat{\mathbf{u}}_2. \quad (5)$$

Denoting $e^{\mathbf{C}t} = \mathbf{A}(t)$, formal integration of (5) yields

$$\hat{\mathbf{u}}_2(t) = \mathbf{A}(t) \hat{\mathbf{u}}_2(0) \equiv e^{-i\omega t} \hat{\mathbf{u}}_2(0). \quad (6)$$

The eigenspectrum of the matrix exponential, $\mathbf{A}(t)$, dictates the time evolution of the eigenfunctions of $\mathbf{A}(t)$. The real and imaginary parts of ω provide the frequency (ω_r) and growth rate (ω_i) of disturbances, respectively. Instead of an explicit computation of the eigenvalues of the large, two-dimensional stability problem, an iterative method is used following Sorensen [14]. In this method, eigenvalues with the highest growth rates, and also those that yield phase speeds similar to that extracted from DNS, are extracted with the implicitly restarted Arnoldi method (IRAM). The Francis QR factorization technique is used to extract eigenvalues. The L^2 norm is used to scale the eigenfunctions. A fuller description of the iterative scheme is provided in Hack and Zaki [3] and is not repeated here.

Formally, the iterative eigenvalue solver applies the linear vector differential operator $\mathbf{A}(t)$ repeatedly to an initial disturbance field as in (6). In practice, this is equivalent to repeatedly integrating (1) and (2) in time, with the boundary conditions (3) and (4). Time integration is with a fractional step method, similar to the solution scheme used for the DNS: advection uses the second order Adams Bashforth scheme, and diffusion uses the implicit Crank Nicolson scheme [7]. The spatial discretizations in both wall-normal and spanwise directions is by second-order central differencing. For both the momentum equation and the pressure correction steps, periodicity in the spanwise direction is exploited by solving for coefficients of spanwise Fourier modes, followed by an inverse transform. 161 and 482 grid points are used to discretize the equations in the wall-normal and spanwise directions, respectively.

An important consideration is the calculation of the frequency of the instability mode [Eq. (6)]

$$\omega_r \Delta t = -\theta, \quad (7)$$

where, θ is the phase of a complex eigenvalue of $\mathbf{A}(t)$, and Δt is the interval of time integration. The iterative scheme is based on most unstable mode dominating at large times. Care is needed in choosing Δt , as an inverse trigonometric function is required to compute the modal frequency. Δt was chosen in conjunction with applying $\mathbf{A}(t)$ multiple times, to ensure $|\omega_r \Delta t| \sim \pi/4$ which is within the range of the inverse trigonometric function used.

The instantaneous base flow, from the DNS, incorporates the full nonlinear evolution of the boundary layer populated by instability waves and Klebanoff streaks. A series of base states is extracted from DNS by streamwise displacement of the sampling plane at the phase speed of the disturbance observed in DNS. In this way, evolution of a helical disturbance from quasiparallel stability analysis can be compared, in an approximate sense, to DNS.

III. RESULTS & DISCUSSION

In the mixed mode transition regime, the primary flow field is a juxtaposition of Kelbanoff streaks and instability waves on the boundary layers. In the APG simulations, the instability waves arise spontaneously [8], while in ZPG, an unstable TS wave is injected at the inlet of the simulation domain.

First, consider the phenomenology seen in DNS. Figure 1(a) depicts the primary disturbance field at three time instants, from the APG simulation with $Tu = 1\%$. Instantaneous isosurfaces of streamwise perturbation velocity u' are shown along with the contours of wall-normal perturbation

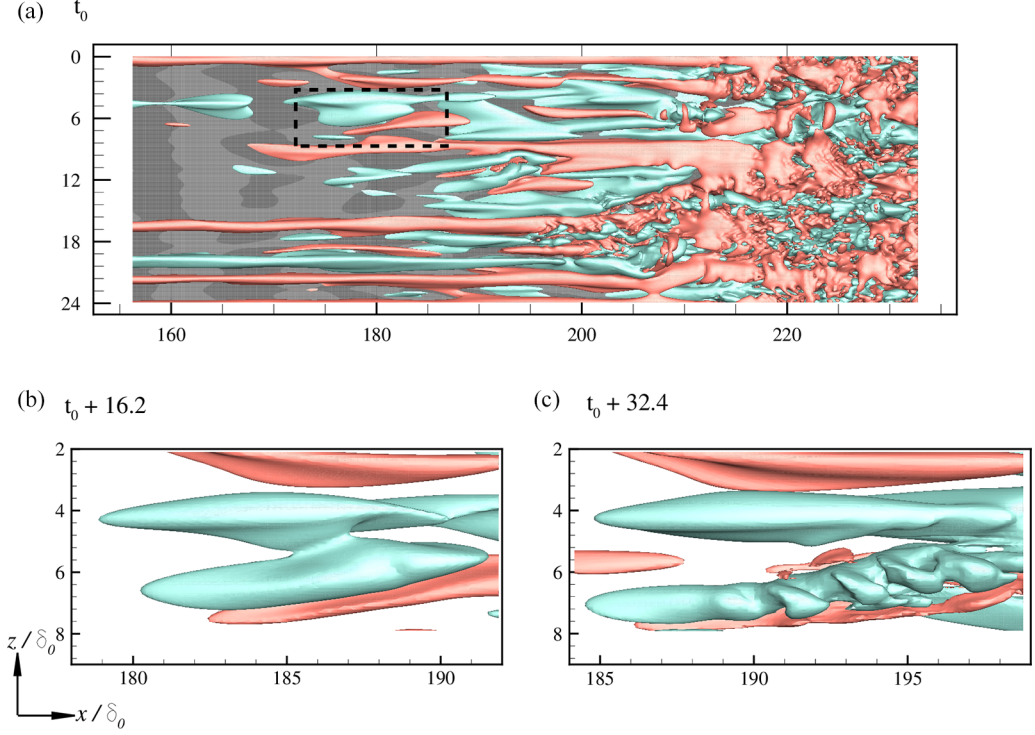


FIG. 1. Top view of the surfaces of isostreamwise perturbation velocity, u' (red and green indicate high- and low-speed regions, respectively) at three time instants from the DNS of APG boundary layer with $Tu = 1\%U_\infty$ listed in Table I: (a) $u' = \pm 0.06$; Contours of $-0.2 \leq v' \leq 0.2$ (darker is negative) at a wall-parallel plane at $y = 0.5\delta_0$. (b) and (c) $u' = \pm 0.1$.

velocity, v' , at a wall-parallel plane $y/\delta_0 = 0.5$. While the streaks are prominent in the isosurfaces of u' , the instability waves are identifiable in v' . Although the contours of v' are shown at a wall normal height where the instability wave amplitude is close to its maximum amplitude [7,8], the streaks and instability waves interact throughout the thickness of the boundary layer.

The streaks are locally distorted by the instability waves and form local patches of mixed mode precursors. The low-speed streaks, for example, are locally reinforced by the negative streamwise perturbation due to the instability waves and vice versa. This results in local thickening and thinning of the streaks in the spanwise direction. The precursors therefore have a streamwise size corresponding to the wavelength of the instability waves. In general, the mixed mode precursors form on the low-speed streaks which become the seat for the helical instability. The black dashed box encloses one such precursor. Once this precursor forms, it amplifies much faster than both the streaks and instability waves, spawning the helical instability, which breaks down quickly to form a turbulent spot. The development of the precursor, formation of the helical instability, and breakdown take place over a short streamwise distance of $10 - 20\delta_0$ as shown in Figs. 1(b) and 1(c). The streamwise size of the precursor is $\sim 10\delta_0$, while the wavelength of the helical instability is $\sim 1.3-2\delta_0$. How the mixed mode precursor originates is beyond the scope of the current paper.

A yz plane extracted at $x/\delta_0 \sim 185.8$ at the same time instant, $t_0 + 16.2$, as Fig. 1(b) is shown in Fig. 2. Figure 2(a) shows the full spanwise extent of the domain; a zoomed-in view of the precursor on which the helical instability develops is presented in Fig. 2(b). Figure 2(b) includes contours of the streamwise perturbation eigenfunction corresponding to the eigenmode with the highest growth rate computed via (2) for this base flow configuration.

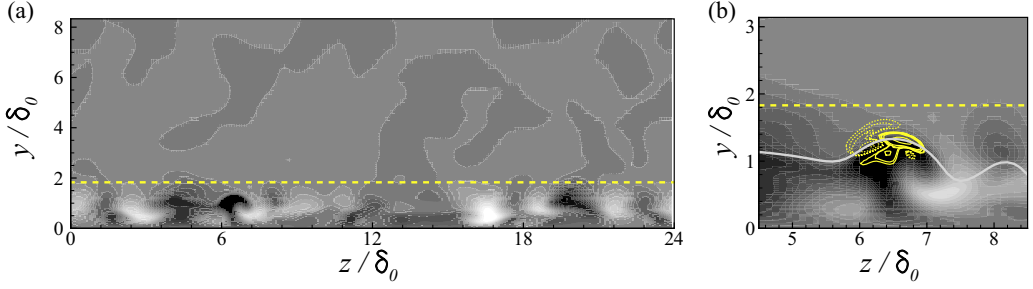


FIG. 2. Contours of $-0.2 \leq u' \leq 0.2$ (dark for negative values) at time $t_0 + 16.2$ as in Fig. 1(b) at the streamwise location $x/\delta_0 \sim 185.8$: (a) The full spanwise domain is shown; (b) Zoomed-in view of the helical mode precursor. The yellow contours show the real part of the streamwise perturbation eigenfunction, u'_2 (dashed lines indicate negative values). The light gray solid line and the horizontal yellow dashed line mark the local critical layer and δ_{99} , respectively.

k_x is an input parameter of the stability calculation. It is estimated from the helical instability in the snapshot shown in Fig. 1(c). It is evident that the instability develops on a high-amplitude, mushroomlike, low-speed streaky structure. Unlike the inner varicose instability described by Hack and Zaki [3], which forms when a high-speed streak climbs up a low-speed streak from behind, the inner helical instability forms when a low-speed structure overlaps a high-speed structure from the side (also see Fig. 2 in [6]). The low phase speed, $c \approx 0.546$ of this instability mode confirms that the helical mode is an inner instability. The critical layer for the instability is shown in Fig. 2(b).

xy planes through a helical mode [6,7] reveal a Kelvin-Helmholtz type instability which is similar in description to the inner varicose mode. However, unlike the inner varicose modes [3], Fig. 2(b) shows that the low-speed structure positions on top of the high-speed structure for a helical mode.

Figure 3 is a three-dimensional view of velocity components of the most unstable eigenmode, over two streamwise wavelengths (the unstable wavelength, $\lambda_x/\delta_0 = 1.55$). This clearly reveals a helical pattern. It is quite distinct from the previously reported sinuous and varicose type instabilities [2]. Among these, the outer sinuous- and inner varicose-type instabilities dominate at high $Tu \geq 3\%U_\infty$. The wavelengths and phase speeds of the outer sinuous instabilities are significantly larger than the inner instabilities [3]. Although the inner varicose-type instabilities have similar wavelengths and phase speeds as the helical modes, their mode shape is different. For comparison, a three-dimensional view of perturbation velocity components of an inner varicose-type eigenfunction computed from a base flow field extracted from the APG simulation with $Tu = 2\%U_\infty$ (although both inner helical- and varicose-type modes are obtained for this case, the helical mode is dominant [8]) is presented in Fig. 4. The phase speed of this mode is $c \approx 0.53$, and the wavelength is $\lambda_x/\delta_0 = 2$; these are similar to the helical mode presented in Fig. 3. The mode shape is similar to that reported by Hack and Zaki [3], however, it is very different from the inner helical mode.

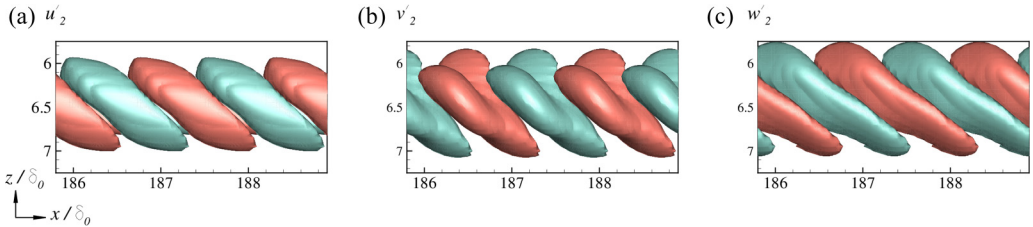


FIG. 3. Top view of the isosurfaces of perturbation eigenfunctions (red and green represent positive and negative perturbation, respectively) for the most unstable mode from stability analysis plotted over two wavelengths: (a) $u'_2 = \pm 0.02$, (b) $v'_2 = \pm 0.015$, (c) $w'_2 = \pm 0.02$.

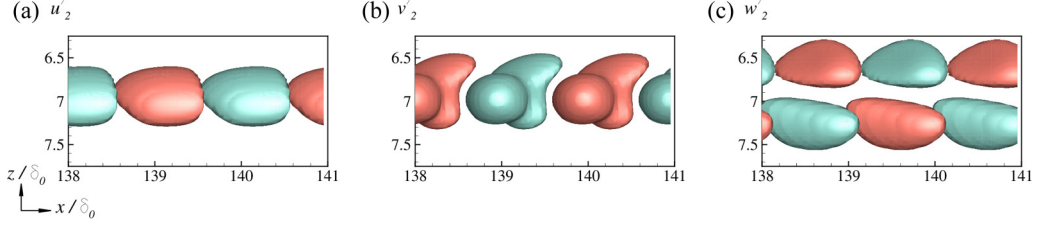


FIG. 4. Top view of the isosurfaces of perturbation eigenfunctions (red and green represent positive and negative perturbation, respectively) for an inner varicose-type mode from stability analysis plotted over one and half wavelengths: (a) $u'_2 = \pm 0.025$, (b) $v'_2 = \pm 0.015$, (c) $w'_2 = \pm 0.02$.

The disturbance field from the stability calculations is in qualitative agreement with the helical mode observed in the DNS of Fig. 1(c). The chirality of the helix depends on the direction of the sidewise overlap of the low- and the high-speed streaks. For this particular instance of the helical mode, the overlap is from the right of the low-speed streak, and therefore, looking downstream, the helix wraps clockwise around the low-speed streak. In cases where it is on the left, the helical instability rotates counterclockwise.

Although the most unstable helical eigenmode (hereafter called mode 1) is shown in Figs. 2 and 3, the stability analysis predicts multiple unstable modes for base states like that shown in Fig. 2. The phase speed, c , and the temporal growth rate, ω_i , for the three most unstable modes of the two base states extracted at time instants $t_0 + 16.2$ (Fig. 2) and $t_0 + 27$ (at this instant, the helical instability is about to become prominent in DNS) are plotted against the streamwise perturbation wavelength, λ_x/δ_0 , in Fig. 5. The second most unstable mode (mode 2) has phase speed similar to mode 1. However, its growth rate is lower for all λ_x/δ_0 . For mode 1, the highest value of ω_i is obtained for $\lambda_x/\delta_0 \sim 1.25$ at $t_0 + 16.2$, and for $\lambda_x/\delta_0 \sim 1.55$ at $t_0 + 27$. Therefore, the stability analysis predicts an increase in the streamwise wavelength of the helical instability with downstream distance. This is qualitatively consistent with the DNS. The third most unstable mode (mode 3) has a significantly lower phase speed than modes 1 and 2, and is stable for all λ_x/δ_0 at inception of the helical instability, $t_0 + 27$. At the earlier instant, $t_0 + 16.2$, this mode is unstable for $\lambda_x/\delta_0 > 1.5$. The mode shapes for modes 2 and 3 are presented in the Appendix.

The stability analysis was performed on a series of base states extracted from DNS following the evolution of the helical mode. The streamwise wavelength for the stability analysis is $\lambda_x/\delta_0 = 1.55$, for which ω_i was highest at $x/\delta_0 \sim 185.8$ and $t = t_0 + 16.2$ (see Fig. 5), and is approximately the streamwise average wavelength of the helical mode in DNS. The results (phase speed and growth

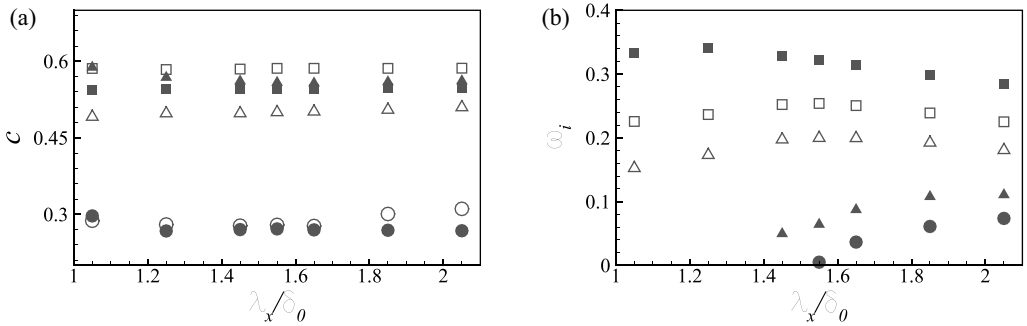


FIG. 5. (a) Phase speed, c , and (b) growth rate, ω_i , plotted against streamwise wavelength, λ_x/δ_0 , for the three most unstable modes for base states extracted from DNS at $t_0 + 16.2$ and $x/\delta_0 \sim 185.8$ (filled symbols), and at $x/\delta_0 \sim 190.2$ and $t_0 + 27$ (blank symbols): \square , most unstable, \triangle , second most unstable, and \circ , third most unstable modes.

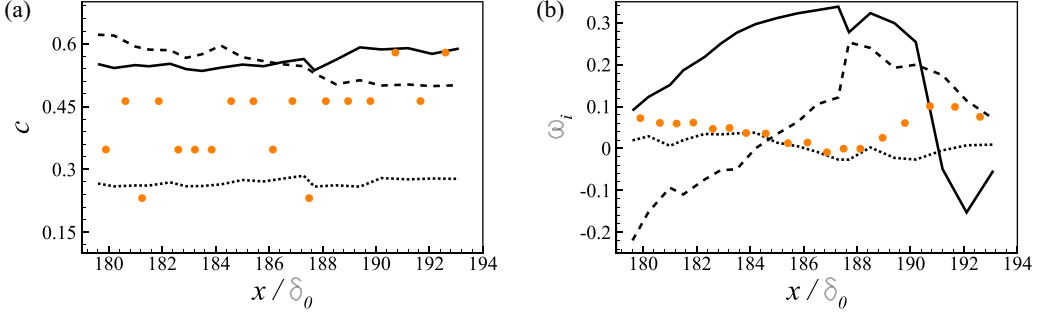


FIG. 6. Streamwise evolution of a helical instability from DNS (symbols) and stability analysis, —, mode 1; - - - -, mode 2; · · · · ·, mode 3: (a) Phase speed; (b) Growth rate.

rate) are compared with those extracted from DNS in Fig. 6. Phase speed is extracted from the DNS data by following the helical mode precursor backward in time and applying a finite difference formula. The spatiotemporal growth rate is extracted by following the peak of v' corresponding to the instability in a wall-parallel plane located at $y/\delta_0 = 1$ (the plane is close to the critical layer obtained for the inner helical mode shown in Fig. 2) and using the formula

$$\omega_{\text{DNS}}^i = \frac{1}{\Delta t} \ln \left| \frac{v'(t' + \Delta t)}{v'(t')} \right|.$$

In Fig. 6(a), phase speeds extracted from DNS show four discrete levels, indicating a superposition of instabilities propagating downstream. The phase speed of the unstable modes from stability analysis remains approximately constant with downstream distance.

The superposition of the unstable modes obtained from stability analysis has some elements of consistency with the DNS. The growth rate ω_i for the helical mode is significantly larger than those extracted from DNS. The temporal growth rate of mode 3 is in good agreement with the DNS, but this mode has a smaller phase speed than those extracted from the DNS. Mode 2 is initially stable, and only becomes unstable at $x/\delta_0 \sim 184.2$. Note that, as shown in Fig. 2, the helical mode is the most unstable well before it becomes clearly seen, at $t_0 + 27$ and $x/\delta_0 \approx 192$. Its high growth rate means that the time interval between its inception and breakdown is very short. In DNS's, the breakdown of the helical mode after its genesis is also very short; it can only be clearly identified in isosurface plots at $t_0 + 27$, and it breaks down at $\sim t_0 + 36$.

In Fig. 6, the growth rate of the most unstable helical mode does not match with those extracted from DNS. There are two reasons: first, the stability analysis is linear, disturbances are monochromatic, and the growth rate is only temporal. The DNS is nonlinear and the growth rate is spatiotemporal. Second, and perhaps more importantly, the length and time scales of the helical instability are an order of magnitude smaller than the base-state instability waves (the scales of the Klebanoff streaks are even larger). Therefore, at the beginning of the transition region, the scales corresponding to the helical instability have negligible energy. Once they become unstable, their energy grows at an exponential rate. Hence, although the helical mode is the most unstable, at first, the primary instability has most of the disturbance energy and dominates the growth rate observed in the DNS. As the disturbance energy at the helical-mode scales become of similar magnitude as the primary instability, they show up in the flow fields, but quickly break down to turbulence. This has been previously verified by plotting spectra, e.g., Fig. 17 in [8].

Helical mode in ZPG

Bose and Durbin [6] also observed the helical mode in a ZPG boundary layer, exposed to free-stream turbulence and a Tolmein-Schlichting wave. The stability results for this case is presented

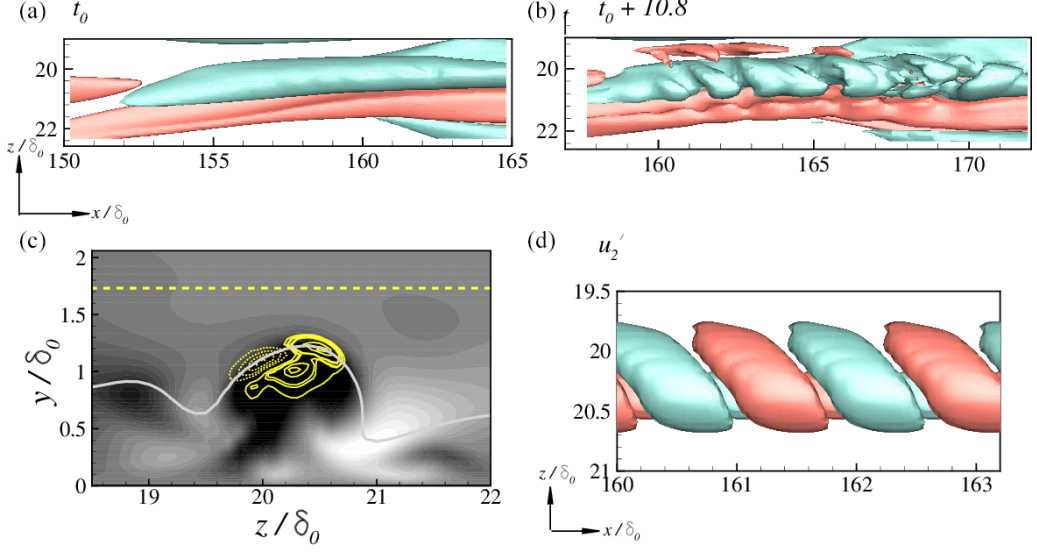


FIG. 7. Evolution of a helical instability in ZPG ($Tu = 1\%$ and $A = 0.5\%U_\infty$): (a) Isosurfaces of $u' = \pm 0.1$ at t_0 and (b) at $t_0 + 10.8$. (c) Contours of $-0.2 \leq u' \leq 0.2$ (dark for negative values) at time t_0 and $x/\delta_0 \sim 160$. The yellow contours show the real part of u'_2 for the most unstable eigenmode (dashed lines indicate negative values). The gray solid line and the horizontal yellow dashed line mark the local critical layer and δ_{99} . (d) Top view of the isosurfaces of $u'_2 = \pm 0.025$ (red and green represent positive and negative perturbation, respectively) for this mode plotted over two wavelengths.

in Fig. 7. It can be hypothesized that an inflectional base flow is not necessary for the inception of helical instability.

Figure 7(a) shows the base flow configuration at time t_0 in a case for which a helical instability was noticed at $t_0 + 10.8$ in the DNS—see Fig. 7(b). The cross-stream plane in Fig. 7(c) shows that the base streak configuration leading to the genesis of a helical mode is the same as that previously described for APG (Fig. 2). The most unstable helical eigenfunction, 7(c), is also similar to the APG case. The eigenmode is obtained for an input $\lambda_x/\delta_0 = 1.6$ which is similar to the average wavelength of the helical instability seen in Fig. 7(b). The eigenmode from the stability analysis corresponds to $c \approx 0.624$, and $\omega_i \approx 0.39$. The phase speed and growth rates extracted from DNS at this streamwise station are $c \sim 0.63$ and $\omega_i \sim 0.01$. These results are also consistent with the analysis presented for APG. Figure 7(d) shows the top view of surfaces of iso- u'_2 values depicting the helical mode in ZPG.

IV. CONCLUSIONS

The fundamental question addressed in this paper is whether the helical patterns that have been seen in flow visualizations of mixed mode transition can be traced to an underlying instability. That has been shown to be the case. An instability was found that is distinct from the sinuous and varicose secondary instability modes that have previously been cited in studies of bypass transition. The helical secondary instability is peculiar to mixed mode transition—that is, when precursors consist of a combination of Klebanoff streaks and instability waves. Stability analyses were performed for base states extracted from DNS of mixed mode transition in both APG and ZPG boundary layers. Those base states are unstable to modes of a helical form. Why these base states occur in the mixed mode regime remains an open question.

The stability analyses predict either two or three unstable modes, of which the helical, inner mode has the highest growth rate. Helical instability occurred significantly earlier than where helices were detected in DNS, indicating that it is the underlying cause.

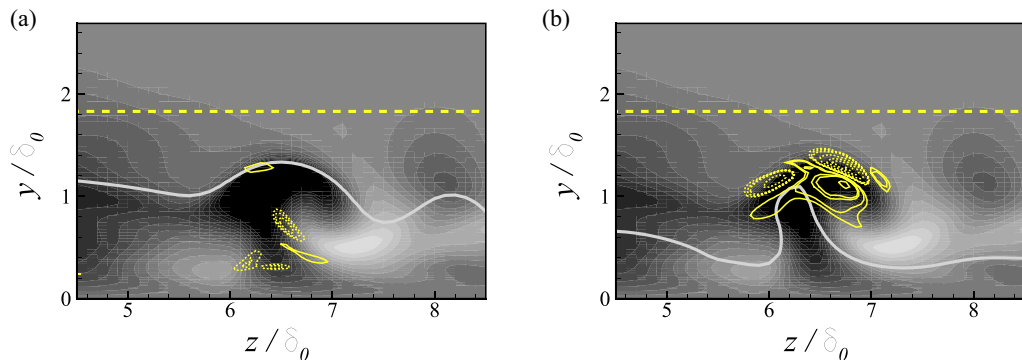


FIG. 8. Contours of real part of the streamwise perturbation eigenfunction (dashed lines indicate negative values) for the (a) second and (b) third most unstable modes at time $t_0 + 16.2$ as in Fig. 2(b) at the streamwise location $x/\delta_0 \sim 185.8$. The gray solid line and the horizontal yellow dashed line mark the local critical layer and δ_{99} , respectively.

The growth rate predicted by the stability analysis for the helical mode is larger compared to that extracted from DNS. This too is evidence that the instability gives rise to the observed vortical structures. The initial disturbance grows rapidly, but has small amplitude. Thus, it is swamped by higher amplitude features seen in the DNS. As the energy of the helical mode becomes larger than the primary instability, helices appear in the DNS flow fields, and quickly break down to turbulence.

ACKNOWLEDGMENT

Part of the work was performed by R.B. while supported by the NIST director's postdoctoral fellowship, which is gratefully acknowledged.

APPENDIX: UNSTABLE MODES

The stability analysis predicts three unstable modes as the mixed mode precursor shown in Fig. 1 develops downstream (Fig. 6). The eigenfunction of the most unstable helical mode (mode 1) is shown in Figs. 2 and 3.

Figure 8 shows the in-plane structure of the eigenfunctions of modes 2 and 3 in the same cross-stream (yz) plane and at the same time instant as in Fig. 2. The real part of u'_2 is shown as in Fig. 2(b) for the helical mode. Mode 2 is active around the stem of the mushroomlike low-speed streaky mixed mode precursor. Mode 3 on the other hand is also very similar to the helical mode, although, with a relatively deeper critical layer. The phase speeds of modes 2 and 3 are 0.558 and 0.27, respectively.

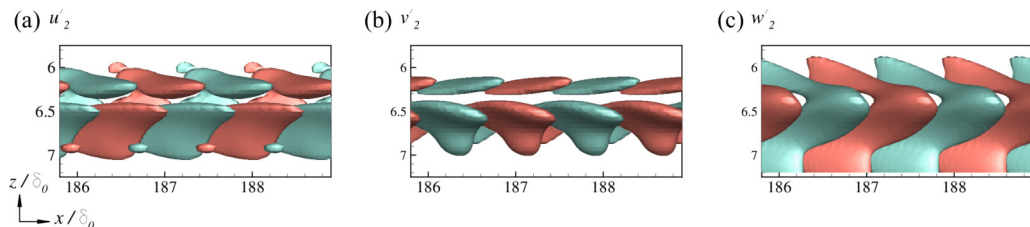


FIG. 9. Top view of the isosurfaces of perturbation eigenfunctions (red and green represent positive and negative perturbation, respectively) for the second most unstable mode from stability analysis: (a) $u'_2 = \pm 0.0075$, (b) $v'_2 = \pm 0.005$, (c) $w'_2 = \pm 0.006$.

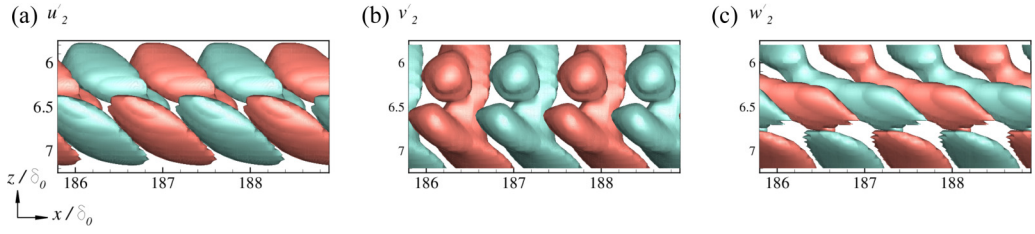


FIG. 10. Top view of the isosurfaces of perturbation eigenfunctions (red and green represent positive and negative perturbation, respectively) for the third most unstable mode from stability analysis: (a) $u'_2 = \pm 0.012$, (b) $v'_2 = \pm 0.01$, (c) $w'_2 = \pm 0.012$.

The three-dimensional structure of modes 2 and 3 are presented over two streamwise wavelengths in Figs. 9 and 10. Mode 2 has a symmetrical appearance. Mode 3 on the other hand is helical in appearance. The three-dimensional structure of u'_2 for this mode appears to be similar to that of a helix with a higher azimuthal wave number than mode 1. v'_2 and w'_2 appears to be symmetric w.r.t. the base streaky structure. In the DNS, the flow structure is likely to be a superposition of the three unstable modes, although the helical mode dominates over a long time (Fig. 1) due to its much higher growth rate.

-
- [1] P. A. Durbin, Perspectives on the phenomenology and modeling of boundary layer transition, *Flow Turbulence Combustion* **99**, 1 (2017).
 - [2] P. Andersson, L. Brandt, A. Bottaro, and D. S. Henningson, On the breakdown of boundary layers streaks, *J. Fluid Mech.* **428**, 29 (2001).
 - [3] M. J. P. Hack and T. A. Zaki, Streak instabilities in boundary layers beneath free-stream turbulence, *J. Fluid Mech.* **741**, 280 (2014).
 - [4] G. J. Walker and J. P. Gostelow, Effects of adverse pressure gradients on the nature and length of boundary layer transition, *J. Turbomachinery* **112**, 196 (1990).
 - [5] K. J. A. Westin, A. V. Boiko, B. G. B. Klingmann, V. V. Kozlov, and P. H. Alfredsson, Experiments in a boundary layer subjected to freestream turbulence. Part I. Boundary layer structure and receptivity, *J. Fluid Mech.* **281**, 193 (1994).
 - [6] R. Bose and P. A. Durbin, Helical modes in boundary layer transition, *Phys. Rev. Fluids* **1**, 073602 (2016).
 - [7] R. Bose and P. A. Durbin, Transition to turbulence by interaction of free-stream and discrete mode perturbations, *Phys. Fluids* **28**, 114105 (2016).
 - [8] R. Bose, T. A. Zaki, and P. A. Durbin, Instability waves and transition in adverse-pressure-gradient boundary layers, *Phys. Rev. Fluids* **3**, 053904 (2018).
 - [9] N. J. Vaughan and T. A. Zaki, Stability of zero-pressure-gradient boundary layer distorted by unsteady Klebanoff streaks, *J. Fluid Mech.* **681**, 116 (2011).
 - [10] R. Bose, Mixed mode transition to turbulence in boundary layers, Ph.D. thesis, Iowa State University, 2016.
 - [11] L. Brandt, P. Schlatter, and D. S. Henningson, Transition in boundary layers subject to free-stream turbulence, *J. Fluid Mech.* **517**, 167 (2004).
 - [12] R. G. Jacobs and P. A. Durbin, Simulations of bypass transition, *J. Fluid Mech.* **428**, 185 (2001).
 - [13] D. Barkley and R. D. Henderson, Three-dimensional Floquet stability analysis of the wake of a circular cylinder, *J. Fluid Mech.* **322**, 215 (1996).
 - [14] D. C. Sorensen, Numerical methods for large eigenvalue problems, *Acta Numerica* **11**, 519 (2002).